

# Intrinsic non-Markovian magnetisation dynamics

Felix Hartmann<sup>\*,1,\*</sup> Vivek Unikandanunni<sup>\*,2,3</sup> Matias Bargheer<sup>1,4</sup>  
Eric E. Fullerton<sup>5</sup> Stefano Bonetti<sup>2,6</sup> and Janet Anders<sup>1,7,†</sup>

<sup>1</sup>*Institute of Physics and Astronomy, University of Potsdam, 14476 Potsdam, Germany*

<sup>2</sup>*Department of Physics, Stockholm University, Stockholm, Sweden*

<sup>3</sup>*Institute of Applied Physics, University of Bern, Sidlerstrasse 5, 3012 Bern, Switzerland*

<sup>4</sup>*Helmholtz-Zentrum Berlin für Materialien und Energie GmbH,*

*Wilhelm-Conrad-Röntgen Campus, BESSY II, 12489 Berlin, Germany*

<sup>5</sup>*Center for Memory and Recording Research, University of California San Diego, San Diego, California 92093, USA*

<sup>6</sup>*Department of Molecular Sciences and Nanosystems,*

*Ca' Foscari University of Venice, 30172 Venice, Italy*

<sup>7</sup>*Department of Physics and Astronomy, University of Exeter, Exeter EX4 4QL, UK*

Memory effects arise in many complex systems, from protein folding [1], to the spreading of epidemics [2] and financial decisions [3]. While so-called non-Markovian dynamics is common in larger systems with interacting components, observations in fundamental physical systems have been confined to specifically engineered cases [4–10]. Here, we report the experimental observation of non-Markovian dynamics in an elemental material, crystalline cobalt. By driving this material with an intense terahertz electromagnetic field, we bring its magnetisation into a non-equilibrium state and follow its evolution. We measure the sample's low temperature magnetic response in the time domain which leads to an unexpectedly rich multi-peaked spectrum in the Fourier domain, that cannot be explained by established models. We use open quantum system theory, which predicts a non-Markovian memory kernel in the dynamical equations to capture the fundamental interaction between the spin system and the phonon bath. Simulations based on this theory produce a multi-peaked spectrum, which matches the measured one. Our non-Markovian approach is also able to reproduce the modification of the spectrum at higher temperatures. Our findings demonstrate that non-Markovian effects are observable at a much more fundamental level than previously thought, opening the door to their exploration and control in a broad range of condensed matter systems.

Damping is an everyday phenomenon, which we experience when we need to pedal to keep a constant speed on a bicycle, or in the movement of an empty swing that climbs less high with every round, finally coming to rest. Microscopically, damping arises from the system continuously interacting with a large number of degrees of freedom, its environment or bath. Such dissipative dynamics is usually one-way: the system will lose energy to the bath and move closer to the rest state, as illustrated for a single pendulum in Fig. 1a. This is known as Markovian dynamics where the bath is memoryless. In contrast, when two individual pendula are coupled to each other, they are able to transfer energy back and forth. Each pendulum then undergoes so-called “non-Markovian” dynamics, where backflow of energy is possible. Much more complex motion then emerges, sometimes towards and sometimes away from the rest state, see Fig. 1b. While for two coupled pendula this behaviour is easy to observe, non-Markovian dynamics can in principle also arise from a system's natural coupling to its dissipative bath.

This requires the bath to play a much more active role; instead of just receiving dissipated energy, it must be able to give energy back. In statistical physics, such dynamics is modeled by a generalised Langevin equation [11], which includes a memory kernel  $K(t - t')$ . This function weights the impact of the past state of the system (at time  $t'$ ) on the current dynamics (at

time  $t$ ). For kernels with short memory times, the dynamics reduces to the standard (Markovian) Langevin equation. For example, protein folding dynamics data has been shown to be matched by models with a non-trivial kernel [1], and methods to accurately infer memory kernels from observed system dynamics have been

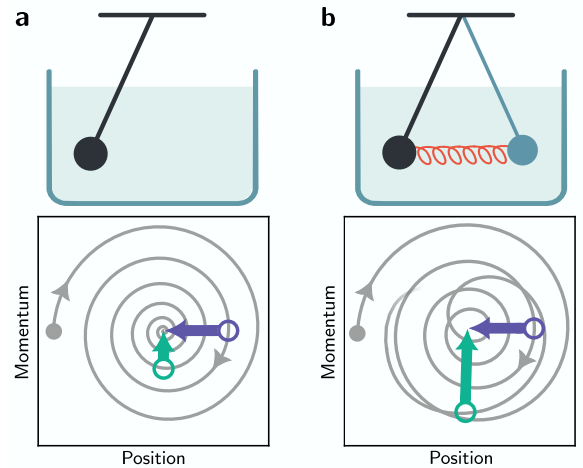


**FIG. 1. Sketch of Markovian vs non-Markovian dynamics.** **a.** A pendulum (black) interacting with its environment (shaded) has a trajectory (grey spiral) in position-momentum space that monotonously moves towards its state of rest, consistent with Markovian dynamics. **b.** In contrast, the trajectory (grey spiral-like) of a single pendulum (black) that interacts (orange spring) with another pendulum, shows complex dynamics with non-Markovian features, such as time excursions away from its state of rest. This is highlighted by the later-time arrow (green) which is longer than the earlier-time arrow (purple), each showing the distance from the state of rest.

\* These authors contributed equally to this work

\* hartmann3@uni-potsdam.de

† janet@qipc.org

developed [12]. Meanwhile, most experiments demonstrating non-Markovianity have been confined to situations akin to the two pendula in Fig. 1b. For example, for a Nitrogen-Vacancy (NV), the dynamics of its electron spin is non-Markovian due to its tunable interaction with the NV centre’s nuclear spin [7], while any remaining bath-influence is demonstrably Markovian. Experimental evidence of non-Markovian dynamics that arises purely from a system’s interaction with a dissipative bath, has only been achieved in rather complex and often highly engineered systems, such as quantum dots in microfabricated nanostructures [4], photon polarisation made to interact with photon frequency in all-optical setups [5], and colloidal particles swimming in polymer enriched viscoelastic baths [10].

Here we report on the discovery of intrinsic non-Markovian signatures in a fundamental condensed matter system: a ferromagnetic cobalt film. The quantity of interest is the magnetisation  $\mathbf{M}$  of the sample, while the bath that damps its dynamics are the natural vibrational excitations of the solid (i.e. phonon bath) [13]. By driving with an intense terahertz pulse, we bring the spin system out of equilibrium and into resonance with the phonon bath with which it can exchange energy. This is the corresponding intrinsic energy scale where the bath does not only damp, but it can also return energy and information back to the system. Our experimental magnetisation signal shows a complex Fourier spectrum with multiple peaks, which are unexplained by established theory, such as the Landau-Lifshitz Gilbert (LLG) equation [14] and the inertial LLG (iLLG) equation [15–20]. To explain the peaks, we advance that the missing conceptual ingredient is the influential role of the bath of lattice vibrations. Taking an open quantum system approach widely used in quantum optics [21, 22], we model the spin interaction with its phononic environment [23]. Parametrising the resulting non-Markovian LLG (nM-LLG) equation with experimental values, we find that the simulated spectrum shows excellent agreement with the experimental spectrum.

### Pump-probe experiment

We perform single-cycle THz pump/time-resolved magneto-optical Kerr effect (MOKE) probe measurements on fcc Co thin film samples at cryogenic temperatures (see Appendix). The film is epitaxially grown on an MgO substrate and exhibits exceptional crystalline quality, which reduces internal damping [24]. The sample lies in the  $x$ - $y$ -plane and is placed in a low-vibration cryostat with windows transparent to both the terahertz pump and the near-infrared probe light. Single-cycle THz pulses are generated using organic crystals that provide highest spectral power density in the 1–3 THz range [25, 26]. The THz magnetic field points along the  $y$ -direction, while the external bias field acts in the  $x$ -direction (see Appendix Fig. 5). The THz pulse excites the spin dynamics, while minimizing thermal effects.

To isolate “magnetic” and “non-magnetic” parts of the signal at low temperatures, where cryostatic con-

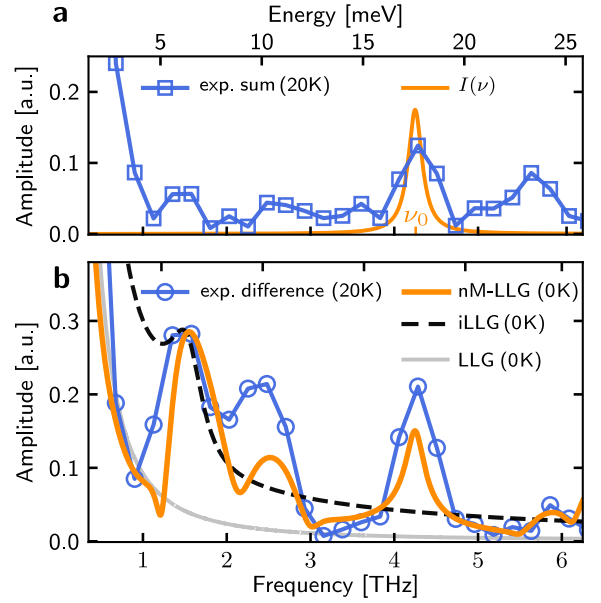


FIG. 2. **Sum and difference spectra of terahertz-induced dynamics in a ferromagnetic cobalt film.** **a.** Fast Fourier transform of summed (non-magnetic) time-resolved signal (blue symbols on solid line) following spin excitation with a strong terahertz pump field. Lorentzian spectral density  $I(\nu)$  (orange solid line) centred at frequency  $\nu_0 = 4.2$  THz to match signal, and with width  $\Gamma = 0.2$  THz, see main text. **b.** Fast Fourier transform of the difference (magnetic) response following the same pump field and at the same temperature (blue symbols on solid line), Fourier spectra of the simulated LLG equation (grey solid line), iLLG equation (black dashed line) and of the nM-LLG equation (orange solid line). nM-LLG simulation solves Eq. (1) with memory kernel  $K(t - t')$  specified by Lorentzian spectral density  $I(\nu)$ , with fixed parameters  $\nu_0$ ,  $\mathcal{A}$  and  $\Gamma$ , see main text. Units for amplitudes of the experimental and simulation spectra are chosen such that the peak amplitudes at 1.4 THz coincide.

finement makes switching the polarity of the bias magnetic dc field [18, 27] impossible, we instead take two traces with flipped polarity of the terahertz pump field ( $\pm\mu_0 H_{\text{THz}} \hat{\mathbf{y}}$ ), see Appendix Fig. 7. By crosschecking this method’s difference signal with that obtained with the standard method [18], both at room temperature, their equivalence is confirmed experimentally. This difference (antisymmetric) signal isolates response components that are odd with respect to the THz field, which are primarily magnetic signatures. In contrast, the sum signal is dominated by non-magnetic contributions, such as phonon excitations. Thus, this approach provides selective access to signals primarily associated with magnetic (difference) and non-magnetic (sum) parts of sample’s response. Identifying the non-magnetic part, i.e. oscillatory features observed on sub-10-ps timescales, is important for parametrising the bath, as discussed below.

Typical time traces for the sum and difference signal, measured at temperature  $T_{\text{exp}} = 20$  K, are shown in Appendix Fig. 8. Taking the fast Fourier transform (FFT) of each, we first plot in Fig. 2a the magnitude of the FFT of the non-magnetic contribution. The data reveal the presence of two peaks at 4.2 THz and 5.7 THz. This signal evidences phonon activity linked to the non-

equilibrium magnetisation dynamics, and the specific frequencies match the zone edge frequencies of the  $\Gamma-L$  and  $\Gamma-X$  phonons in fcc cobalt, respectively [28, 29] (see Appendix).

Fig. 2b shows the FFT of the magnetic part of the signal. It reveals a rich terahertz spectrum with three rather unexpected pronounced peaks. Until recently, modelling of magnetisation signals has been accomplished with the LLG equation [14], a phenomenological and Markovian theory describing precession and damping. However, it does not predict any such peaks. Extending the LLG theory by including the angular momentum degree of freedom was proposed by Ciornei, Rubí and Wegrowe [15] resulting in the so-called inertial LLG equation, or iLLG. This inertial theory [19] predicts a single, much faster rocking motion on top of the precession, which is typically observed in the GHz range in ferromagnets. In previous experiments [17, 18], good agreement between the iLLG's single inertial peak and one of the experimentally observed peaks, corresponding to our peak at about 1.4 THz, was observed. However, the pronounced additional peaks that were observed in Ref. [18], and that we now observe at 2.4 THz and 4.2 THz, cannot be described by either the LLG or iLLG equations.

Recently a non-Markovian LLG equation has been put forward, derived using an open quantum systems approach which models system and bath together [23]. In Fig. 2b we plot the Fourier spectrum of the magnetic response simulated with the nM-LLG equation as the orange solid line on top of the experimental data. It is immediately obvious that the nM-LLG simulation naturally produces an initial valley followed by multiple spectral peaks. Moreover, the quantitative match with the experimentally observed peak frequencies is outstanding. Simulation details are given in Appendix. We note that simulations depend on three kernel parameters which are obtained from the experimental data, see below.

### Non-Markovian kernel

The nM-LLG equation arises from coupling the spin system to the phonon bath via an interaction term  $V_{\text{int}} = \mathbf{M} \cdot \int_0^\infty d\nu \sqrt{\nu I(\nu)} \mathbf{X}_\nu$  where  $\mathbf{M}$  is the magnetisation of the sample,  $\mathbf{X}_\nu$  is the position coordinate of the phonon bath mode at frequency  $\nu$ , and  $I(\nu)$  is the bath spectral density which characterises the strength of coupling of the spin system to various bath frequencies  $\nu$ . Solving the set of coupled equations for the magnetic system and the phonons results in the nM-LLG equation

$$\dot{\mathbf{M}}(t) = \mathbf{M}(t) \times \left[ \gamma \mathbf{H}_{\text{eff}}(t) + \int_{t_0}^t dt' K(t-t') \mathbf{M}(t') \right], \quad (1)$$

where  $\mathbf{M}(t)$  is the magnetisation at time  $t$ ,  $|\gamma|/2\pi = 28$  GHz/T,  $\mathbf{H}_{\text{eff}}(t)$  is the effective magnetic field consisting of an external bias field  $\mathbf{H}_{\text{bias}} = 0.1 \text{ T } \hat{\mathbf{x}}$  and a demagnetisation field  $\mathbf{H}_d(t)$  which acts substantially only along the  $z$ -direction (i.e. out-of-plane) in a thin film and is proportional to  $M_z(t)$ .

The non-Markovian nature of Eq. (1) is made explicit by the presence of the memory kernel  $K(t-t')$ . Its significance is to link the dynamics at time  $t$ , to the magnetisation vector  $\mathbf{M}(t')$  at previous times  $t'$ . The strength and temporal extent of this memory is determined by the exact shape and parameters of the kernel. Physically, these parameters are fixed by the bath properties [30]. Knowing the bath spectral density  $I(\nu)$  determines the memory kernel [23],  $K(t-t') = 2\pi \int_0^\infty d\nu I(\nu) \sin(2\pi\nu(t-t'))$  for  $t \geq t'$ . Spectral densities can be approximated with a Lorentzian shape [23],  $I(\nu) = \mathcal{A}\Gamma\nu/((\nu_0^2 - \nu^2)^2 + \Gamma^2\nu^2)$ , which centers around a dominant frequency  $\nu_0$ .  $\Gamma$  and  $\mathcal{A}$  specify the range of frequencies where coupling is significant and the overall strength of the coupling, respectively. Zone-boundary and transverse acoustic phonons can carry energy and angular momentum in ultrafast demagnetisation experiments [29, 31, 32]. Therefore, they can act as the energy and angular momentum bath in ultrafast spin dynamics.

Hence, in order to identify  $I(\nu)$  for the sample measured, we return to the frequencies seen in the non-magnetic signal in Fig. 2a. We identify the peak at 4.2 THz as that corresponding to states occupied by zone-boundary transverse acoustic phonons [28]. This naturally fixes the center frequency of the sample's Lorentzian spectral density  $I(\nu)$  to  $\nu_0 = 4.2$  THz. The remaining two Lorentzian parameters are obtained via known identities [23]  $\alpha = \mathcal{A}\Gamma/\nu_0^4$  and  $\tau_{\text{in}} = (\nu_0^2 - \Gamma^2)/(2\pi\nu_0^2\Gamma)$ . Here  $\alpha$  and  $\tau_{\text{in}}$  are the damping parameter and the inertial time, previously found [18] by fitting the first peak in the experimental signal with the iLLG equation giving  $\alpha = 0.15$  and  $\tau_{\text{in}} = 0.8$  ps. This fixes the kernel parameters  $\Gamma = 0.2$  THz and  $\mathcal{A} = 242.0$  THz<sup>3</sup> (Appendix). Numerical simulation of Eq. (1), including the memory kernel  $K$  while not adding thermal noise (i.e. 0 K), produces the orange line in Fig. 2b.

The match between fully parameterised theory and experiment (at 20 K) demonstrates that the spin system undergoes dynamics described by the non-Markovian LLG equation (1), which includes a temporally extended memory kernel. This non-Markovianity directly arises on the fundamental scale of the spins interacting with their phonon bath.

### Analytic reasoning for multiple peaks

We now give an analytic explanation for the appearance of multiple spectral peaks. Returning to the nM-LLG equation (1) it is instructive to Taylor expand the magnetisation  $\mathbf{M}(t')$  around time  $t$  leading to multiple derivatives of  $\mathbf{M}(t)$ , i.e.

$$\dot{\mathbf{M}}(t) = \mathbf{M}(t) \times \left[ \gamma \mathbf{H}_{\text{eff}}(t) + \sum_{m=1}^{\infty} \kappa_m \partial_t^m \mathbf{M}(t) \right]. \quad (2)$$

The derivatives are weighted by the coefficients  $\kappa_m = (-1)^m \int_0^\infty d\zeta \zeta^m K(\zeta)/m!$ , which are the  $m$ -th one-sided moments of the memory kernel [23]. The standard LLG equation [14] is captured by this description when only the first derivative (i.e.  $m = 1$ ) is included,

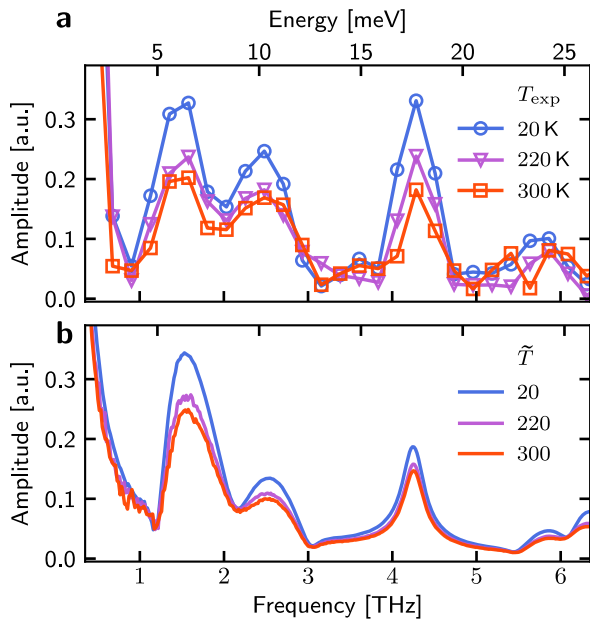


FIG. 3. **Temperature dependence of THz-frequency spectrum.** **a.** Fourier transform of experimental signal at three temperatures,  $T_{\text{exp}} = 20$  K (blue line, circles),  $T_{\text{exp}} = 220$  K (purple line, triangles) and  $T_{\text{exp}} = 300$  K (red line, squares). The three experimental spectra were measured with a single THz polarity, and contain magnetic and non-magnetic contributions. **b.** Fourier transform of dynamics obtained by solving the nM-LLG equation for three different unit-free temperatures  $\tilde{T} \propto T_{\text{exp}}$  chosen at the same ratios as in the experiment. Simulations of the nM-LLG equation (1) include coloured thermal noise, and the demagnetisation field is reduced for higher temperatures, see Appendix. Scale of the  $\tilde{T} = 20$  graph in **b** is chosen such that first peak amplitude matches the experimental one in **a**. Amplitudes at higher temperatures follow relatively from it. All remaining simulation parameters are identical to Fig. 2.

which makes it Markovian by construction [11, 33]. This approach also describes correctly the iLLG equation [15] which is the Taylor expansion up to the second derivative ( $m = 2$ ); see also [34] where inertial damping is identified as a higher order spin-orbit coupling effect. Thus, the iLLG equation can be seen as a truncated Taylor expansion of the full non-Markovian description. We note that microscopic models resulting in additional fractional derivatives in Eq. (2), which also lead to non-Markovian dynamics, have also been proposed [35, 36].

The full expansion of the nM-LLG equation highlights the presence of higher order derivatives in the time-domain. It has previously been argued [37] that expressing the dynamics in the frequency domain, and by identifying the roots of the resulting frequency-polynomial, gives insight into where additional peaks are expected. The LLG ( $m = 1$ ) and iLLG ( $m = 2$ ) equations produce one and two roots, respectively, which are identified as the precession and the inertial peak. In contrast, the memory kernel  $K$  in the nM-LLG equation (1) naturally leads to the presence of higher derivatives in (2). Hence if nature is described by Eq. (1), one would expect multiple peaks in the MOKE spectrum (see Appendix).

## Variation with temperature

To complete the description of the bath-coupled dynamics, we finally explore the impact of temperature variation on the non-Markovian dynamics, i.e. variation of the population of vibrational modes in the bath. The experimentally measured spin dynamics at three temperatures,  $T_{\text{exp}} = 20$  K,  $T_{\text{exp}} = 220$  K, and  $T_{\text{exp}} = 300$  K, is presented in the Fourier domain in Fig. 3a (for the temporal traces see Appendix Fig. 9). We observe that the frequencies of the spectral peaks remain fixed. Meanwhile, the peak amplitudes decrease when the temperature of the sample is increased.

We now examine the expected temperature dependence arising from the nM-LLG equation (1). It incorporates thermal fluctuations via the inclusion of a thermal field  $\mathbf{h}_{\text{th}}(t)$  in  $\mathbf{H}_{\text{eff}}(t)$ , which stochastically fluctuates in time [23]. Additionally, the demagnetisation field is reduced at increased temperatures [38], see Appendix.

The noise  $\mathbf{h}_{\text{th}}(t)$  has, via fluctuation-dissipation theorem, the power spectral density  $P(\nu) = 2k_{\text{B}}T_{\text{exp}}I(\nu)$ , which introduces the experimental sample temperature  $T_{\text{exp}}$  while  $k_{\text{B}}$  is the Boltzmann constant. Within the macrospin approximation, precise information on the number of spins, their individual moments and their interactions is not available, which leaves the absolute temperature scale undetermined. Here we choose an absolute scale by setting the unit-free version of the simulation temperature,  $\tilde{T}$ , to  $\tilde{T} = T_{\text{exp}}/K$ , which fixes the relative temperature ratios thereafter. With temperature now included in the simulation of the nM-LLG equation (1), the THz-frequency spectrum for three temperatures,  $\tilde{T} = 20$ ,  $\tilde{T} = 220$  and  $\tilde{T} = 300$ , is shown in Fig. 3b. As can be seen, the frequencies of the peaks remain fixed, while their relative amplitudes reduce with increasing temperature. The qualitative agreement with the experimental data in Fig. 3a is also impressive.

## Conclusion and outlook

The discovery that the collective dynamics of spins in a piece of ferromagnet cannot be described by the usual one-way damped motion is a major change of perspective for our understanding of condensed matter systems. In the new picture, the phonon bath plays a much more active role, not solely receiving dissipation from the spin system, but also giving energy back. Such backflow occurs because the phonon bath, which interacts with the spin system, imprints an intrinsic non-Markovian memory kernel on the spin dynamics. Theory also allows to estimate the kernel's memory time [23], i.e. the extent of a system's memory of its past, here  $\tau_{\text{memory}} = 2/\Gamma \approx 10$  ps. This natural picosecond memory time is much shorter than the time-period of precession in typical ferromagnetic resonance experiments, which is in the nanosecond regime. On this slower timescale the coupling of the spins to the bath reduces to conventional damping, and non-Markovian effects cannot be observed, as illustrated in Fig. 4a. In contrast, when non-equilibrium spin dynam-



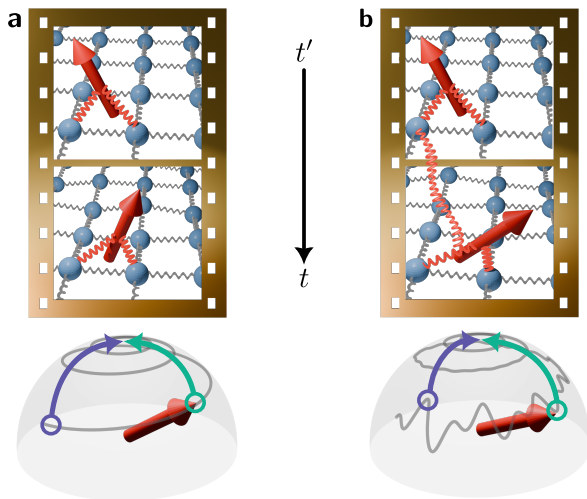


FIG. 4. **Illustration of Markovian and non-Markovian spin dynamics.** **a.** Markovian dynamics: the magnetisation (red arrow) is coupled only to the instantaneous state of the phonon bath (connected grid) at each frame in time  $t'$  and  $t$ . Viewed on the Bloch sphere, the magnetisation uniformly spirals towards its rest state (cf. Fig. 1a). **b.** Non-Markovian dynamics: the magnetisation at a later time  $t$  is coupled (red spring) also to the spin state at an earlier time  $t'$ . Viewed on the Bloch sphere, the magnetisation dynamics exhibits a complex behavior (grey trajectory). The presence of higher frequency dynamics leads to spin excursions away from its state of rest (green arrow), a clear non-Markovian characteristic. In the Fourier domain, such complex motion presents in the form of multiple THz-frequency spectral peaks as seen in Fig. 2 and 3.

ics is excited in the THz range, as was done here, its timescale becomes of the same order as the bath's imprinted memory time. Without time-scale separation, the past states of the spin influence its future dynamics, as illustrated in Fig. 4b. The measurable effect is a complex motion of the magnetisation at these time scales, which in the frequency domain shows up as multiple peaks in the THz regime.

We anticipate the presented findings to be of broader general validity, and to apply to the description of coupled collective dynamics in solids where measurements can be performed on the same timescale as the relevant memory kernel. In the terahertz regime, this is expected to happen, for instance, in nonlinear phononics experiments, where phonons can exchange energy and angular momentum [39–41], while in the gigahertz regime, non-trivial kernels could be present in coupled magnon-phonon dynamics [42]. Theoretical models predict non-Markovian signatures in the absorption spectra of monolayers of transition metal dichalcogenides, which feature strong exciton-phonon interaction [43]. Future experiments may also investigate predictions that non-Markovian baths can enable faster routes to stationarity [44]. Considerable system-bath interactions promise a range of applications, such as improved control of system dynamics via the environment. Application areas include phonon-assisted coherent control of a single color center in van der Waals materials [45], and reducing decoherence in quantum

technologies with bath-engineering techniques [9]. Non-Markovian baths are also expected to be important for control applications with atomic scale probes on surfaces [46] as well as reducing environmental noise in quantum sensing with single spins [46–48].

By exciting and detecting dynamics on ultrashort timescales, our experiment opens new avenues for the exploration of regimes where the inanimate world of solids exhibits dynamics reminiscent of living systems, and where the monotonic growth of entropy no longer holds [49, 50]. Identifying the right scales and mechanisms to observe such behaviour in other platforms will be a key next step.

## ACKNOWLEDGMENTS

We thank Fried-Conrad Weber and Tobias Kampfrath for discussions on the topic. JA thanks Simon Horsley for anticipating a connection between [17] and [23]. We thank Brendon Lovett for comments on an early draft of the manuscript. S.B. acknowledges support from the Italian Ministry of University and Research. This study was carried out within the PRIN 2022 cod. 2022ZRLA8F, and received funding from the European Union Next-GenerationEU - National Recovery and Resilience Plan (NRRP) – MISSION 4 COMPONENT 2, INVESTIMENT 1.1 Fondo per il Programma Nazionale di Ricerca e Progetti di Rilevante Interesse Nazionale (PRIN) – CUP: H53D23000890006. VU acknowledges the support of the SNSF Sinergia project (CRSII5 213533). MB acknowledges funding by the Deutsche Forschungsgemeinschaft (DFG, German Research Foundation) – TRR 227 – Project-No. 328545488, project A10. JA acknowledges support from EPSRC grant EP/R045577/1, and the Royal Society. FH and JA acknowledge support from the DFG, grants 513075417 and 384846402. JA and MB acknowledge funding by the DFG, grant 510943930 (CRC1636).

## CONTRIBUTIONS

J.A. conceived the initial idea, which was further developed by F.H., V.U., S.B. and J.A. F.H. performed and analyzed the simulations. S.B. and V.U. designed and conducted the experiments, and analysed the data. E.F. fabricated the samples. F.H., V.U. and J.A. wrote the first draft of the manuscript. M.B. contributed key points to the interpretation of the observations. All authors discussed the results and commented on the manuscript. S.B. and J.A. supervised the project.

## DATA AVAILABILITY

The data supporting the findings of this study are available upon reasonable request from the corresponding authors.

- [1] C. Ayaz, L. Tepper, F. N. Brünig, J. Kappler, J. O. Daldrop, and R. R. Netz, Non-markovian modeling of protein folding, *Proc. Natl. Acad. Sci. U.S.A.* **118**, (31) e2023856118 (2021).
- [2] M. T. Sofonea, B. Reyné, B. Elie, R. Djidjou-Demasie, C. Selinger, Y. Michalakakis, and S. Alizon, Memory is key in capturing covid-19 epidemiological dynamics, *Epidemics* **35**, 100459 (2021).
- [3] J. A. Wachter and M. J. Kahana, A retrieved-context theory of financial decisions, *Q. J. Econ.* **139**, 1095–1147 (2023).
- [4] K. H. Madsen, S. Ates, T. Lund-Hansen, A. Löffler, S. Reitzenstein, A. Forchel, and P. Lodahl, Observation of non-markovian dynamics of a single quantum dot in a micropillar cavity, *Phys. Rev. Lett.* **106**, 233601 (2011).
- [5] B.-H. Liu, L. Li, Y.-F. Huang, C.-F. Li, G.-C. Guo, E.-M. Laine, H.-P. Breuer, and J. Piilo, Experimental control of the transition from markovian to non-markovian dynamics of open quantum systems, *Nat. Phys.* **7**, 931–934 (2011).
- [6] S. Gröblacher, A. Trubarov, N. Prigge, G. D. Cole, M. Aspelmeyer, and J. Eisert, Observation of non-markovian micromechanical brownian motion, *Nat. Commun.* **6**, 7606 (2015).
- [7] J. Haase, P. Vetter, T. Unden, A. Smirne, J. Roskopf, B. Naydenov, A. Stacey, F. Jelezko, M. Plenio, and S. Huelga, Controllable non-markovianity for a spin qubit in diamond, *Phys. Rev. Lett.* **121**, 060401 (2018).
- [8] A. Potočník, A. Bargerbos, F. A. Y. N. Schröder, S. A. Khan, M. C. Collodo, S. Gasparinetti, Y. Salathé, C. Creatore, C. Eichler, H. E. Türeci, A. W. Chin, and A. Wallraff, Studying light-harvesting models with superconducting circuits, *Nat. Commun.* **9**, 904 (2018).
- [9] M. Odeh, K. Godeneli, E. Li, R. Tangirala, H. Zhou, X. Zhang, Z.-H. Zhang, and A. Sipahigil, Non-markovian dynamics of a superconducting qubit in a phononic bandgap, *Nat. Phys.* **21**, 406–411 (2025).
- [10] F. Ginot and C. Bechinger, Energy recuperation of driven colloids in non-markovian baths, *Nat. Commun.* **16** (2025).
- [11] S. A. Loos and A. Godec, Non-markovian effects in nonequilibrium systems, *J. Phys. A* **58**, 220301 (2025).
- [12] L. Tepper, B. Dalton, and R. R. Netz, Accurate memory kernel extraction from discretized time-series data, *J. Chem. Theory Comput.* **20**, 3061–3068 (2024).
- [13] M. Strungaru, M. O. A. Ellis, S. Ruta, O. Chubykalo-Fesenko, R. F. L. Evans, and R. W. Chantrell, Spin-lattice dynamics model with angular momentum transfer for canonical and microcanonical ensembles, *Phys. Rev. B* **103**, 024429 (2021).
- [14] M. Lakshmanan, The fascinating world of the landau–lifshitz–gilbert equation: an overview, *Philos. Trans. R. Soc. A* **369**, 1280–1300 (2011).
- [15] M.-C. Ciornei, J. M. Rubí, and J.-E. Wegrowe, Magnetization dynamics in the inertial regime: Nutation predicted at short time scales, *Phys. Rev. B* **83**, 020410 (2011).
- [16] Y. Li, A.-L. Barra, S. Auffret, U. Ebels, and W. E. Bailey, Inertial terms to magnetization dynamics in ferromagnetic thin films, *Phys. Rev. B* **92**, 140413 (2015).
- [17] K. Neeraj, N. Awari, S. Kovalev, D. Polley, N. Zhou Hagström, S. S. P. K. Arekapudi, A. Semislova, K. Lenz, B. Green, J.-C. Deinert, I. Ilyakov, M. Chen, M. Bawatna, V. Scalera, M. d’Aquino, C. Serpico, O. Hellwig, J.-E. Wegrowe, M. Gensch, and S. Bonetti, Inertial spin dynamics in ferromagnets, *Nat. Phys.* **17**, 245–250 (2020).
- [18] V. Unikandanunni, R. Medapalli, M. Asa, E. Albisetti, D. Petti, R. Bertacco, E. E. Fullerton, and S. Bonetti, Inertial spin dynamics in epitaxial cobalt films, *Phys. Rev. Lett.* **129**, 237201 (2022).
- [19] R. Mondal, L. Rózsa, M. Farle, P. M. Oppeneer, U. Nowak, and M. Cherkasskii, Inertial effects in ultrafast spin dynamics, *J. Magn. Magn. Mater.* **579**, 170830 (2023).
- [20] A. De, J. Schlegel, A. Lentfert, L. Scheuer, B. Stadtmüller, P. Pirro, G. von Freymann, U. Nowak, and M. Aeschlimann, Magnetic nutation: Transient separation of magnetization from its angular momentum, *Phys. Rev. B* **111**, 014432 (2025).
- [21] S. M. Barnett and P. M. Radmore, *Methods in Theoretical Quantum Optics*, Oxford Series in Optical and Imaging Sciences, Vol. 15 (Clarendon Press, 1997).
- [22] B. Huttner and S. M. Barnett, Quantization of the electromagnetic field in dielectrics, *Phys. Rev. A* **46**, 4306 (1992).
- [23] J. Anders, C. R. J. Sait, and S. A. R. Horsley, Quantum brownian motion for magnets, *New J. Phys.* **24**, 033020 (2022).
- [24] T. J. Li and L. Bellon, Dissipation of micro-cantilevers as a function of air pressure and metallic coating, *EPL* **98**, 14004 (2012).
- [25] C. P. Hauri, C. Ruchert, C. Vicario, and F. Ardana, Strong-field single-cycle thz pulses generated in an organic crystal, *Appl. Phys. Lett.* **99** (2011).
- [26] M. Jazbinsek, U. Puc, A. Abina, and A. Zidansek, Organic crystals for thz photonics, *Appl. Sci.* **9**, 882 (2019).
- [27] M. Hudl, M. d’Aquino, M. Pancaldi, S.-H. Yang, M. G. Samant, S. S. Parkin, H. A. Dürr, C. Serpico, M. C. Hoffmann, and S. Bonetti, Nonlinear magnetization dynamics driven by strong terahertz fields, *Phys. Rev. Lett.* **123**, 197204 (2019).
- [28] R. Lizárraga, F. Pan, L. Bergqvist, E. Holmström, Z. Gercsi, and L. Vitos, First principles theory of the hcp-fcc phase transition in cobalt, *Sci. Rep.* **7**, 3778 (2017).
- [29] V. Shokeen, M. Heber, D. Kutnyakhov, X. Wang, A. Yaroslavlsev, P. Maldonado, M. Berritta, N. Wind, L. Wenthaus, F. Pressacco, C.-H. Min, M. Nissen, S. K. Mahatha, S. Dziarzhytski, P. M. Oppeneer, K. Rosnagel, H.-J. Elmers, G. Schönhense, and H. A. Dürr, Real-time observation of non-equilibrium phonon-electron energy and angular momentum flow in laser-heated nickel, *Sci. Adv.* **10**, eadj2407 (2024).
- [30] S. Nemati, C. Henkel, and J. Anders, Coupling function from bath density of states, *EPL* **139**, 36002 (2022).
- [31] C. Dornes, Y. Acremann, M. Savoini, M. Kubli, M. J. Neugebauer, E. Abreu, L. Huber, G. Lantz, C. A. F. Vaz, H. Lemke, E. M. Bothschafter, M. Porer, V. Esposito, L. Rettig, M. Buzzzi, A. Alberca, Y. W. Windsor, P. Beaud, U. Staub, D. Zhu, S. Song, J. M. Glowina, and S. L. Johnson, The ultrafast einstein–de haas effect, *Nature* **565**, 209–212 (2019).
- [32] P. Maldonado, T. Chase, A. Reid, X. Shen, R. Li, K. Carva, T. Payer, M. Horn von Hoegen, K. Sokolowski-Tinten, X. Wang, *et al.*, Tracking the ultrafast nonequilibrium energy flow between electronic and lattice degrees of freedom in crystalline nickel, *Phys. Rev. B* **101**, 100302 (2020).

- [33] I. de Vega and D. Alonso, Dynamics of non-markovian open quantum systems, *Rev. Mod. Phys.* **89**, 015001 (2017).
- [34] R. Mondal, M. Berritta, A. K. Nandy, and P. M. Oppeneer, Relativistic theory of magnetic inertia in ultrafast spin dynamics, *Phys. Rev. B* **96**, 024425 (2017).
- [35] R. C. Verstraten, T. Ludwig, R. A. Duine, and C. Morais Smith, Fractional landau-lifshitz-gilbert equation, *Phys. Rev. Res.* **5**, 033128 (2023).
- [36] F. Reyes-Osorio and B. K. Nikolić, Bringing light into the landau-lifshitz-gilbert equation: Consequences of its fractal non-markovian memory kernel for optically induced magnetic inertia and magnons, *arXiv:2504.17769 preprint* (2025).
- [37] M. Cherkasskii, M. Farle, and A. Semisalova, Nutation resonance in ferromagnets, *Phys. Rev. B* **102**, 184432 (2020).
- [38] R. F. L. Evans, W. J. Fan, P. Chureemart, T. A. Ostler, M. O. A. Ellis, and R. W. Chantrell, Atomistic spin model simulations of magnetic nanomaterials, *J. Phys. Condens. Matter.* **26**, 103202 (2014).
- [39] O. Minakova, C. Paiva, M. Frenzel, M. S. Spencer, J. M. Urban, C. Ringkamp, M. Wolf, G. Mussler, D. M. Juraschek, and S. F. Maehrlein, Direct observation of angular momentum transfer among crystal lattice modes, *arXiv:2503.11626 preprint* (2025).
- [40] T. F. Nova, A. S. Disa, M. Fechner, and A. Cavalleri, Metastable ferroelectricity in optically strained  $\text{SrTiO}_3$ , *Science* **364**, 1075–1079 (2019).
- [41] R. Mankowsky, A. Subedi, M. Först, S. O. Mariager, M. Chollet, H. T. Lemke, J. S. Robinson, J. M. Glowina, M. P. Minitti, A. Frano, M. Fechner, N. A. Spaldin, T. Loew, B. Keimer, A. Georges, and A. Cavalleri, Nonlinear lattice dynamics as a basis for enhanced superconductivity in  $\text{YBa}_2\text{Cu}_3\text{O}_{6.5}$ , *Nature* **516**, 71–73 (2014).
- [42] C. Berk, M. Jaris, W. Yang, S. Dhuey, S. Cabrini, and H. Schmidt, Strongly coupled magnon–phonon dynamics in a single nanomagnet, *Nat. Commun.* **10** (2019).
- [43] F. Lengers, T. Kuhn, and D. E. Reiter, Theory of the absorption line shape in monolayers of transition metal dichalcogenides, *Phys. Rev. B* **101**, 155304 (2020).
- [44] D. J. Strachan, A. Purkayastha, and S. R. Clark, Non-markovian quantum mpemba effect, *Phys. Rev. Lett.* **134**, 220403 (2025).
- [45] J. A. Preuss, D. Groll, R. Schmidt, T. Hahn, P. Machnikowski, R. Bratschitsch, T. Kuhn, S. Michaelis de Vasconcellos, and D. Wigger, Resonant and phonon-assisted ultrafast coherent control of a single hbn color center, *Optica* **9**, 522 (2022).
- [46] Y. Chen, Y. Bae, and A. J. Heinrich, Harnessing the quantum behavior of spins on surfaces, *Adv. Mater.* **35**, 2107534 (2022).
- [47] X. Zhou, M. Wang, X. Ye, H. Sun, Y. Guo, S. Han, Z. Chai, W. Ji, K. Xia, F. Shi, Y. Wang, and J. Du, Entanglement-enhanced nanoscale single-spin sensing, *Nature* **647**, 883–888 (2025).
- [48] J. Rovny, S. Kolkowitz, and N. P. de Leon, Multi-qubit nanoscale sensing with entanglement as a resource, *Nature* **647**, 876–882 (2025).
- [49] P. Strasberg and M. Esposito, Non-markovianity and negative entropy production rates, *Phys. Rev. E* **99**, 012120 (2019).
- [50] D. J. Skinner and J. Dunkel, Improved bounds on entropy production in living systems, *Proc. Natl. Acad. Sci. U.S.A.* **118**, e2024300118 (2021).
- [51] V. Unikandanunni, *Ultrafast spin, lattice, and electron dynamics in thin metallic films: in the terahertz, near-infrared, and extreme ultraviolet regimes*, Ph.D. thesis, Department of Physics, Stockholm University (2021).
- [52] M. Mansuripur, F. Zhou, and J. K. Erwin, Measuring the wavelength dependence of magnetooptical kerr (or faraday) rotation and ellipticity: a technique, *Appl. Opt.* **29**, 1308 (1990).
- [53] K. Carva, M. Battiato, D. Legut, and P. M. Oppeneer, Ab initio theory of electron-phonon mediated ultrafast spin relaxation of laser-excited hot electrons in transition-metal ferromagnets, *Phys. Rev. B* **87**, 184425 (2013).
- [54] S. Scali, S. Horsley, J. Anders, and F. Cerisola, Spidy.jl: open-source julia package for the study of non-markovian stochastic dynamics, *J. Open Source Softw.* **9**, 6263 (2024).
- [55] M. C. Wang and G. E. Uhlenbeck, On the theory of the brownian motion ii, *Rev. Mod. Phys.* **17**, 323–342 (1945).
- [56] H. Mori, A continued-fraction representation of the time-correlation functions, *Prog. Theor. Phys.* **34**, 399–416 (1965).
- [57] E. Olive, Y. Lansac, M. Meyer, M. Hayoun, and J.-E. Wegrowe, Deviation from the landau-lifshitz-gilbert equation in the inertial regime of the magnetization, *J. Appl. Phys.* **117**, 213904 (2015).
- [58] Movie shows the same FFT picture as Fig. 2b in the main text for the iLLG and nM – LLG equations, but under variation of  $\tau_{\text{in}}$  while keeping  $\alpha$  fixed, *Parameter variation movie - PW: nutation\_spectrum* .

## Appendix A: Experimental Method

We performed single-cycle THz pump-800 nm magneto-optical Kerr effect (MOKE) probe measurements on an epitaxially grown face-centered cubic cobalt sample. The sample was placed in a low-vibration cryostat from Advanced Research Systems, allowing temperature-dependent measurements. To minimize pump field loss, we installed TPX windows from *Tydex* optimized for transmission at THz frequencies. The experimental schematic is shown in the Fig. 5. The magnetization  $\mathbf{M}$  of the sample is saturated along the  $x$ -direction using the field  $\mu_0 \mathbf{H}_{\text{bias}}$  of 100 mT of a permanent magnet mounted inside the cryo chamber on the sample holder. THz pump pulses required to drive the ultrafast magnetization dynamics are generated in the organic crystal OH1 via nonlinear-optical rectification of 1300 nm pulses from an optical parametric amplifier. The THz pulse's electric field is polarized along the  $x$ -direction with a maximum amplitude of 830 kV/cm, while the corresponding magnetic field is polarized along the  $y$ -direction with a maximum amplitude of 280 mT. The pump polarization was chosen to maximize the Zeeman torque on the sample magnetization by the pump pulse. We characterized the THz pump pulse spectrum using electro-optical sampling with a 50  $\mu\text{m}$ -thick GaP crystal. The broadband spectrum of the THz pump is centered at 2 THz with a bandwidth exceeding 1 THz (see Fig. 6). The THz pump and 800 nm probe beams were collinearly incident on the sample at a 45-degree angle. The pump-induced changes in the Kerr rotation angle ( $\Delta\theta_K$ ) were monitored using a balanced detection setup.

At room temperature, magnetic contributions are typically isolated by recording time traces under static dc bias fields of equal magnitude and opposite polarity and taking their difference. This approach relies on an electromagnet to reverse the bias field, and the resulting difference signal selects components that are odd under bias field reversal. Implementing such a scheme inside a cryostat is technically challenging. To overcome this limitation, we keep the bias field constant and reverse the polarity of the THz pump magnetic field. Two time traces are recorded, one for each THz polarity, and their difference isolates the response components that are odd with respect to the THz magnetic field, including the coherent magnetic precession and the concomitant magnetization response [18, 27]. Comparison at room-temperature confirms that the difference signal obtained by THz-polarity reversal closely matches the purely magnetic signal measured from reversing the dc bias field, indicating that the extracted difference signal is predominantly magnetic in origin.

The sum of the two traces isolates the components that are even with respect to the THz field, which include non-magnetic phonon dynamics and other even-order magnetic contributions. The latter are negligible within our experimental time window. Reversal of the THz field polarity is achieved by rotating the THz generation crystal by  $180^\circ$ . This introduces a temporal shift of 165 fs due to crystal-thickness inhomogeneity. The temporal shift is corrected before calculating difference and sum signals.

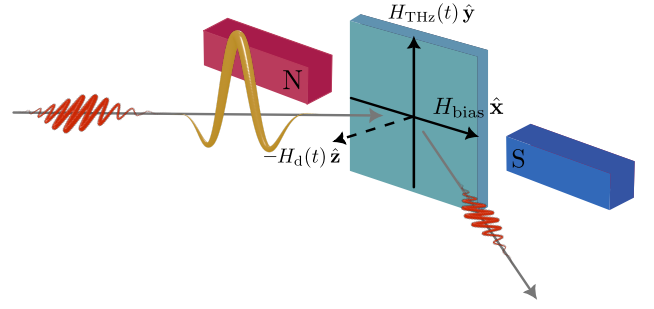


FIG. 5. **Experimental schematic:** THz pump-Magneto-Optical Kerr Effect (MOKE) probe experiment on epitaxial Cobalt thin film. The THz pump and optical probe are collinear with an angle of incidence of 45 degrees. The directions of external bias magnetic field ( $H_{\text{bias}} \hat{x}$ ), THz magnetic field ( $H_{\text{THz}}(t) \hat{y}$ ), and the demagnetizing field ( $-H_d(t) \hat{z}$ ) are shown.

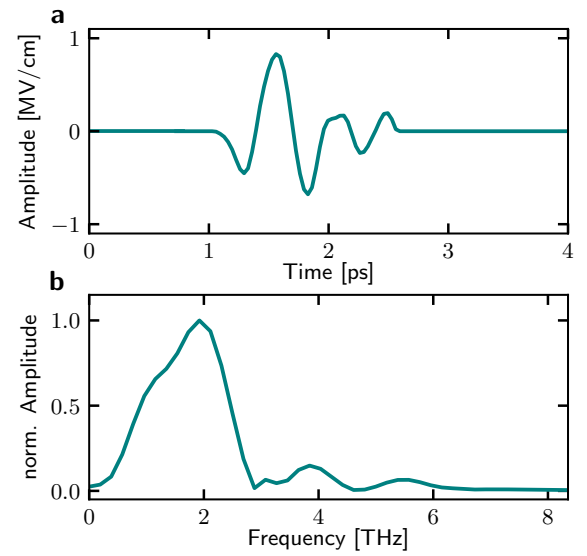


FIG. 6. **Electro-optic sampling of the THz pump pulse:** **a.** Time-domain data: The time trace is zero-padded from 2.7 ps onward to eliminate internal reflections from the thin electro-optic crystal. **b.** Fast Fourier transform of the time-domain signal, revealing the pump spectrum.

## Appendix B: Amplitude of the time-resolved MOKE signal

The time-resolved MOKE signal represents the magneto-optical response, which is proportional to the magnetization dynamics induced by the pump pulse. The relationship between the time-dependent Kerr angle  $\Delta\theta_K$  and the change in magnetization  $\Delta M$  in the weak-perturbation limit is given by

$$\Delta\theta_K(t) = \theta_{K0} \frac{\Delta M(t)}{M_0}, \quad (\text{B1})$$

where  $\theta_{K0}$  is the static magneto-optic Kerr response and  $M_0$  is the total magnetization of the sample [51]. The static Kerr response  $\theta_{K0}$  itself depends on various probe parameters, including but not limited to the probe wavelength, angle of incidence, polarization, and the sample's refractive index at the probe wavelength [52]. Consequently, the absolute magnitude of



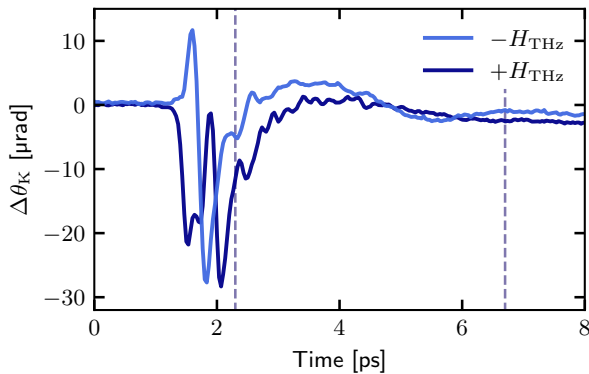


FIG. 7. **Signal for positive and negative polarized pump pulse:** Kerr signal for positive  $+\mu_0 H_{\text{THz}} \hat{y}$  (dark blue solid line) and negative  $-\mu_0 H_{\text{THz}} \hat{y}$  (light blue solid line) polarized pump pulse, respectively.

the experimentally measured magneto-optical response is not intrinsically significant and can vary depending on the probing scheme.

### Appendix C: Sample information

The epitaxial cobalt sample under study has a face-centered cubic (fcc) structure with a thickness of 15 nm. The sample stack, from top to bottom, consists of Pt (5 nm)/Co (15 nm)/Cu (20 nm)/MgO (substrate). The 5-nm-thick platinum layer serves as a cap layer, while the 20-nm-thick copper layer functions as a seed layer for the epitaxial growth on the MgO substrate. Orientation-dependent static magneto-optical characterizations revealed that the sample exhibits minimal magnetocrystalline anisotropy within the plane. In our experiments, the external bias magnetic field was applied along the [100] crystalline direction of the fcc structure. The magnetic field required to saturate the sample magnetization is  $< 100$  mT. Therefore, we applied a field of 100 mT in our experiments to fully align the magnetization along the  $x$ -direction. The static magneto-optical characterization of the sample is detailed in our previous work [18].

### Appendix D: Data Analysis

To perform the Fourier transform, we used time-domain data from a time delay of 2.3 ps to 6.7 ps, where the THz-driven coherent precession has essentially vanished, and the MOKE signal oscillations were clearly visible (See Fig. 8). The data was then multiplied by a Blackman window centered at 4.5 ps with a width of 4.4 ps to minimize spectral leakage. Finally, a Fast Fourier Transform (FFT) was applied to the resulting time-domain signal to obtain the frequency spectrum.

### Appendix E: Sum (non-magnetic) signal and phonon details

As discussed in the main text, we refer to the sum and difference signal of the two THz polarities as non-

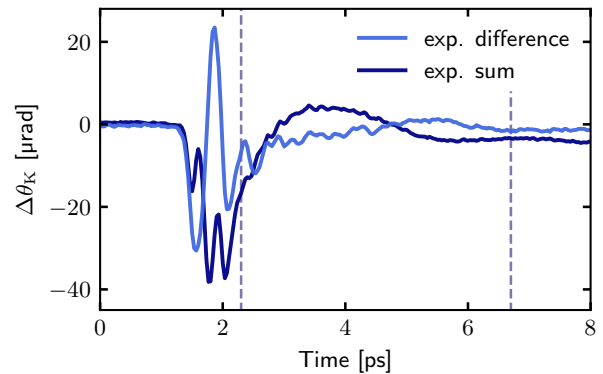


FIG. 8. **Sum and difference time traces:** Time trace obtained by subtracting (magnetic, light blue) and summing (non-magnetic, dark blue) signals, obtained for positive and negative THz pump polarities, respectively, at a temperature of 20 K. The Fourier transforms of the two time traces, for the time window 2.3 – 6.7 ps (dashed lines), are presented in main text Fig. 2a and b.

magnetic and magnetic signal, respectively. The experimentally determined non-magnetic and magnetic contributions at 20 K are shown in Fig. 8. The Fourier transform of the non-magnetic signal, presented in Fig. 2a, reveals an excitation peak at a frequency of 4.2 THz. Here we discuss the physical origin of this signal.

The phonon DOS of fcc Co shows two dominant peaks at approximately 4.2 THz and 8 THz, which are associated with zone-edge transverse and longitudinal acoustic branches, respectively [28, 53]. Recent energy- and momentum-resolved studies have demonstrated the critical role of zone-edge phonons in ultrafast spin-lattice interactions in metallic ferromagnets [29, 32]. In particular, transverse acoustic phonons have been identified as efficient angular momentum sinks on sub-picosecond timescales [31], while longitudinal acoustic phonons, though capable of transporting energy, cannot carry angular momentum and therefore do not contribute significantly to spin-lattice angular momentum transfer. These microscopic mechanisms underscore the unique importance of 4.2 THz transverse acoustic phonons and indicate their active participation in ultrafast spin dynamics.

### Appendix F: Experiments on additional samples

To confirm that the observed dynamics arise from the intrinsic magnetic response of the sample - rather than from spectral structure in the THz pump - we performed complementary measurements on three additional samples using the identical experimental setup. These measurements were carried out at room temperature. Therefore, unlike the low-temperature experiments described in the main text, we isolated the magnetic contribution to the signal by inverting the external bias field instead of the THz polarization. The experimental spectra of all three control samples are shown together in the Fig. 10. The first control sample was a 30-nm-thick epitaxially grown hcp-Co film (blue circles), which exhibits three clear THz spectral peaks

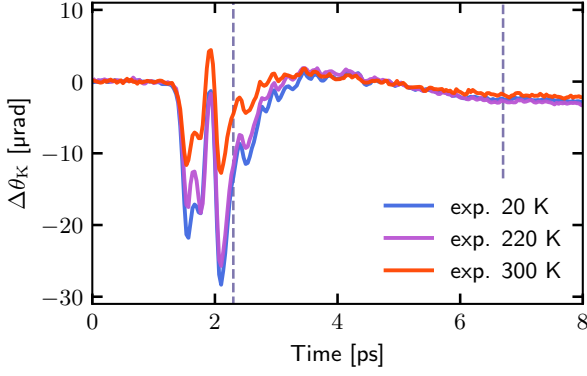


**FIG. 9. Time traces of temperature-dependent magnetization dynamics:** This is for a fixed polarity of THz field, and thus the trace contains magnetic and non-magnetic contributions. In addition to coherent precession (slow oscillation) and THz-frequencies (fast oscillations), a “non-magnetic” response (deep dips around 2 ps) are observed. Spectra shown in main text Fig. 3 are obtained via FFT of the time trace window 2.3 – 6.7 ps.

at 2.1 THz, 3.9 THz, and 5.6 THz, consistent with previous reports [18]. The second sample was a 10-nm-thick epitaxial hcp-Co film (green squares). It shows spectral peaks at approximately the same frequencies, but with amplitudes reduced by roughly a factor of two. This reduction does not scale linearly with thickness because the THz penetration depth in Co ( $\sim 20$  nm) lies between the two sample thicknesses: i.e. the 10 nm film is fully excited, whereas only approximately two-thirds of the 30 nm film participate in the dynamics. Despite the amplitude difference, both epitaxial hcp-Co samples exhibit qualitatively similar behavior that is nonetheless clearly distinct from the response of the epitaxial fcc-Co sample discussed in the main text. The third sample was a 30-nm-thick polycrystalline Co film (yellow triangles). Here, no THz-frequency spectral peaks were detected. This stark contrast with the epitaxial samples highlights that high crystalline quality is essential for observing a coherent, non-Markovian magnetization dynamics. Together, these control measurements demonstrate that the dynamics reported in the main text originate from the sample’s intrinsic magnetization response. The measured behavior depends sensitively on crystal structure and disappears when the crystalline order is reduced.

### Appendix G: Technical simulation details

For the plots in Fig. 2b, all three equations, the LLG, iLLG and nM-LLG simulations are run without stochastic noise, i.e. at zero temperature. The LLG and iLLG simulations are run with the same parameters (i.e. damping, inertial time, initial state) as the nM-LLG simulations to guarantee a fair comparison. The effect of temperature on the observed THz-frequency spectrum for the nM-LLG equation is discussed in the main text (cf. Fig. 3b) and further details are given below.

Simulating the iLLG equation follows the same procedure as previously outlined in Refs. [17, 18]. The sim-

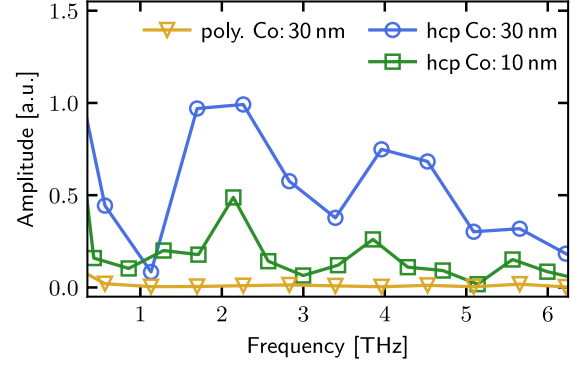


**FIG. 10. FFT of THz pump-MOKE probe measurements of three Co samples:** 30-nm hcp-Co (blue circles), 10-nm hcp-Co (green squares), and 30-nm polycrystalline Co (yellow triangles). The epitaxial hcp-Co samples exhibit distinct THz spectral peaks in the FFT, while the polycrystalline film shows no resolvable peaks. All three measurements are performed at room temperature.

ulation of the nM-LLG equation is done via the open-source software SPiDY [54], which simulates a dimensionless version of Eq. (1). To rerun the simulation, one needs to input the simulation time  $\tilde{t} = \tilde{\omega}_L t$  and the Lorentzian parameters,  $\tilde{\mathcal{A}} = 8\pi^3 \mathcal{A} / \tilde{\omega}_L^3 \simeq 1.1 \cdot 10^7$ ,  $\tilde{\omega}_0 = 2\pi\omega_0 / \tilde{\omega}_L \simeq 151.7$ , and  $\tilde{\Gamma} = 2\pi\Gamma / \tilde{\omega}_L \simeq 7.21$ . These are scaled via an effective Larmor frequency  $\tilde{\omega}_L$ , which is defined for a fixed field strength  $|\mathbf{H}| = 1.0$  T, thus,  $\tilde{\omega}_L = |\gamma| \cdot 1 \text{ T} \approx 1.76 \cdot 10^{11} \text{ rad/s}$ , with  $|\gamma| \approx 1.76 \cdot 10^{11} \text{ rad/s/T}$  being the electron gyromagnetic ratio. This effective Larmor frequency  $\tilde{\omega}_L$  is solely used to transfer the dimensioned experimental parameters given in the main text into dimensionless simulation parameters, and vice versa. The *real* Larmor frequency  $\omega_L$  of the simulated system is set by the effective magnetic field strength  $\omega_L = \gamma|\mathbf{H}_{\text{eff}}|$ , see Eq. (1).

The simulation incorporates the magnetic fields, where the effective field can be written as the following sum

$$\mathbf{H}_{\text{eff}}(t) = (H_{\text{bias}} + H_K)\hat{\mathbf{x}} + H_{\text{THz}}(t)\hat{\mathbf{y}} + H_d(t)\hat{\mathbf{z}}. \quad (\text{G1})$$

In the experiment, the external bias field  $H_{\text{bias}} = 100$  mT is applied along the  $x$ -direction. We neglect the anisotropy field  $H_K$ , as it is small for the fcc Co sample compared to the other magnetic field components [18]. The demagnetization field is given by [27]

$$\mathbf{H}_d(t) = -N_{x,0}M_x(t)\hat{\mathbf{x}} - N_{y,0}M_y(t)\hat{\mathbf{y}} - N_{z,0}M_z(t)\hat{\mathbf{z}}, \quad (\text{G2})$$

where  $N_{x,0}$ ,  $N_{y,0}$ , and  $N_{z,0}$  are the demagnetization field factors. The normalized spin vector components are  $\mathbf{M}(t) = (M_x(t), M_y(t), M_z(t))$ . Here, we have  $N_{x,0} = N_{y,0} = 0$  and  $N_{z,0} = 1.37$  T, therefore, Eq. (G2) reduces to  $\mathbf{H}_d = -N_{z,0}M_z(t)/M_0 \hat{\mathbf{z}}$ , where  $M_0$  is the length of the macrospin, see Fig. 5. For a detailed numerical and experimental study of the above defined demagnetization field, see Ref. [27]. Our non-equilibrium dynamics simulations start once the THz-pulse field has pushed the spin out of equilibrium. Thus, the THz field in the simulation is off,  $H_{\text{THz}}(t) = 0$ , while we set the initial conditions to  $\mathbf{M}(0) = (\sqrt{0.98}, \sqrt{0.02}, 0.0)$  (cf. section below on the initial state).

We numerically integrate the mLLG equation, transforming the integro-differential equation (1) into a system of first-order coupled differential equations [23, 54],

$$\begin{aligned}\frac{d\mathbf{M}(t)}{dt} &= \mathbf{M}(t) \times \left( \mathbf{H}_{\text{eff}} + \frac{1}{\sqrt{M_0}} \mathbf{h}_{\text{th}}(t) + \mathbf{V}(t) \right), \\ \frac{d\mathbf{V}(t)}{dt} &= \mathbf{W}(t), \\ \frac{d\mathbf{W}(t)}{dt} &= -\nu_0^2 \mathbf{V}(t) - \Gamma \mathbf{W}(t) + \mathcal{A} \mathbf{M}(t),\end{aligned}\quad (\text{G3})$$

here  $|\mathbf{M}(0)|$  is assumed to be normalized.  $\mathbf{V}(t)$  and  $\mathbf{W}(t)$  are dummy vectors to incorporate the memory kernel  $\mathcal{K}(t - t')$ . Mathematically, this step is known as Markovian embedding, where the full non-Markovian dynamics is solved via coupled Markovian equations [55, 56]. This introduces the need for nine initial conditions (three for  $\mathbf{M}$  and three for  $\mathbf{V}$  and  $\mathbf{W}$ ), compared to three or six for the LLG or iLLG equation, respectively. To simplify, we set  $\mathbf{V}(0) = \mathbf{0}$  and  $\mathbf{W}(0) = \mathbf{0}$ , representing an initial state without memory effects or momentum in the auxiliary variables. We choose  $\mathbf{M}(0)$  slightly out of equilibrium to model realistic dynamics, where the system is perturbed from perfect alignment, as typical for pump-probe experiments when the pump pulse has passed.

Similarly to the amplitude of the time-resolved MOKE signal, see above, the *absolute* amplitude of the simulated THz-frequency spectrum is not directly informative. It depends, e.g., on the time-step choice and the exact initial conditions. For visualization purposes, we here chose the amplitudes of the experimental and simulation spectra such that their first THz-frequency peak amplitudes match, as seen in Fig. 2b.

### Appendix H: Parameter variation

We here compare the robustness of the obtained frequency spectra for the iLLG and nM-LLG equation for changes in the inertial time  $\tau_{\text{in}} = 0.8$  ps. For changes of  $\pm 5\%$  the spectra are shown in Fig. 11. We observe that the frequency of the *single* inertial peak in the spectrum of the iLLG equation is inversely proportional with  $\tau_{\text{in}}$ , as previously reported e.g. in Ref. [57]. Likewise we find that the lowest frequency peak in the THz range in the spectrum of the nM-LLG equation changes; however, the change is more pronounced and other parts of the spectrum change as well. The frequency peak at 4.2 THz is very robust. This arises because the non-magnetic  $\nu_0$  enters as a parameter in the memory kernel, see Eq. (J1), which hence oscillates with  $\nu_1 = \sqrt{\nu_0^2 - \Gamma^2/4} \approx \nu_0$ , for  $\Gamma \ll \nu_0$ . A movie, showing the change of the THz-frequency spectrum arising from the nM-LLG-equation when it is solved for different inertial times  $\tau_{\text{in}}$  while holding  $\alpha$  and  $\nu_0$  fixed ( $\mathcal{A}$  and  $\Gamma$  are changed accordingly) is available at [58]. We note that the specific THz-frequency spectrum is quite sensitive to variation, both experimentally [17] and theoretically, see Fig. 11. This points at the reasons of why it has been rather difficult for the community to measure THz-frequency spectra. Despite the parameter-sensitivity of the detailed spectrum, we highlight that

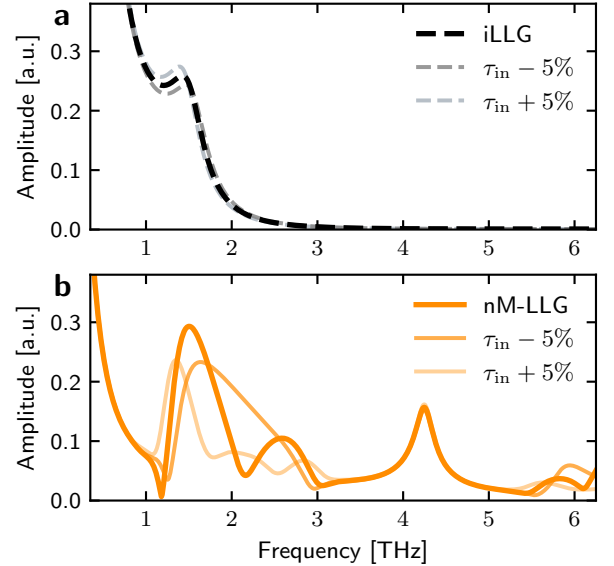


FIG. 11. **Parameter varied spectrum.** Thick lines show spectra identical to Fig. 2b while the more transparent lines show changes of the spectra when the inertial time  $\tau_{\text{in}}$  is varied by  $\pm 5\%$ . In **a**, the simulation of the iLLG equation and in **b**, the simulation of the nM-LLG equation.

the theory consistently predicts, for a wide range of Lorentzian parameters, a structured multi-peak spectral THz-frequency response. This indicates the possibility to characterize the THz-frequency spectrum of other ferromagnetic materials in the future.

### Appendix I: Multiple THz-frequencies predicted by susceptibility expansion

In the main text we gave a heuristic explanation and numerically demonstrated that the nM-LLG equation (1) produces multiple THz-frequencies. Here we provide an even more detailed analytical explanation for their appearance, following the approach proposed in [37].

The magnetic response arises from the memory-kernel  $K(t - t')$  in Eq. (1), which is Taylor expanded in Eq. (2). The effective field  $\mathbf{H}_{\text{eff}}(t)$  is specified as in Eq. (1), however, the demagnetization field is neglected for simplicity and we drop the eff index. We wish to find the magnetic response in Fourier picture (indicated by  $\sim$ ); more specifically we wish to find the susceptibility  $\chi_j(\nu)$  which links the field to its response via

$$\tilde{M}_j(\nu) = M_0 \chi_j(\nu) \tilde{H}_j(\nu), \quad (\text{I1})$$

for each spatial component  $j$ . We follow [37] and linearize Eq. (2) by neglecting higher-order products of  $\mathbf{M}$  and  $\mathbf{H}$ . Applying the Fourier transform one obtains

$$\begin{aligned}i\nu \tilde{\mathbf{M}}(\nu) &= -\nu_L \hat{\mathbf{x}} \times \tilde{\mathbf{M}}(\nu) + \hat{\mathbf{x}} \times \tilde{\mathbf{H}}(\nu) \\ &\quad + \hat{\mathbf{x}} \times \sum_{m=1}^{\infty} \kappa_m (i\nu)^m \tilde{\mathbf{M}}(\nu),\end{aligned}\quad (\text{I2})$$

with  $\nu_L = \omega_L/(2\pi) = 2.8$  GHz being the Larmor frequency for the external bias field of  $H_{\text{bias}} = 100$  mT.

Using  $\tilde{M}_\pm = \tilde{M}_z \pm i\tilde{M}_y$  and  $\tilde{H}_\pm = \tilde{H}_z \pm i\tilde{H}_y$ , one arrives at the susceptibility  $\chi_\pm(\omega)$  for positive (+) and negative (−) polarization directions,

$$\chi_\pm(\nu) = \left( \nu_L - \sum_{m=1}^{\infty} \kappa_m (i\nu)^m \pm \nu \right)^{-1}. \quad (\text{I3})$$

This susceptibility  $\chi_\pm(\nu)$  diverges whenever the  $m$ -th order polynomial in Eq. (I3) becomes zero. The absolute values of the real part of these roots give the frequency at which maxima (and also minima) are expected in the Fourier spectrum of the spin dynamics described by Eq. (2).

For the iLLG equation, the damping  $\alpha$  and inertial time  $\tau_{\text{in}}$ , relate to the two expansion coefficients  $\kappa_{1,2}$  in Eq. (2) as  $\kappa_1/M_0 = -\alpha$  and  $\kappa_2/M_0 = -\alpha\tau_{\text{in}}$ . For the parameter values specified above, one analytically finds roots at the precession frequency at 2.8 GHz, and a single spectral THz-frequency at 1.4 THz, consistent with the simulation shown in Fig. 2a. It is well-known, that the iLLG equation can only show a *single* inertial peak, and its frequency has previously been derived Refs. [37, 57].

Now, the memory kernel  $K(t - t')$  in the nM-LLG equation naturally leads to the presence of multiple expansion orders in Eq. (2). This implies higher order polynomials in Eq. (I3), which have a larger number of zeroes. Hence with a memory kernel present in the dynamics, we would analytically expect multiple spectral THz-frequency peaks. Specifically, for our Lorentzian memory kernel, the expansion coefficients  $\kappa_m/M_0$  in Eq. (2) are [23]  $\kappa_m/M_0 = (-1)^m \mathcal{A} / \left( \nu_1 \nu_0^{2(m+1)} \right) \text{Im}[(\Gamma/2 + i\nu_1)^{m+1}]$ , where  $\nu_1 = \sqrt{\nu_0^2 - \Gamma^2/4}$ . While this series never breaks up, the coefficients decay with increasing order. Here we take into account the first six expansion orders. Solving for the zeroes of the sixth order polynomial in Eq. (I3), we find zeroes at 2.8 GHz and 1.23 THz – which are close to the zeroes of the iLLG equation for the precession and the inertial peak, respectively. In addition, we find a (semi-degenerate) frequency at 2.45 THz (and 2.46 THz), which very well matches the second spectral THz-frequency peak found numerically in the spin dynamics, see Fig. 2b. A further (semi-degenerate) zero lies at 1.82 THz (and 1.85 THz), which appears to correspond to a “valley” in Fig. 2b.

Predicting the exact frequencies of the peaks is not reliable, as the above analytical approach is based on several assumptions, including forcing a linearization of Eq. (2). Further untangling the mathematical interplay of non-linear effects together with the memory kernel will be the subject for future research.

## Appendix J: Form of memory kernels in time

In this manuscript we discussed that the nM-LLG equation with its memory kernel is capable to capture the experimentally observed complex frequency spectrum. The kernel of the Lorentzian spectral density

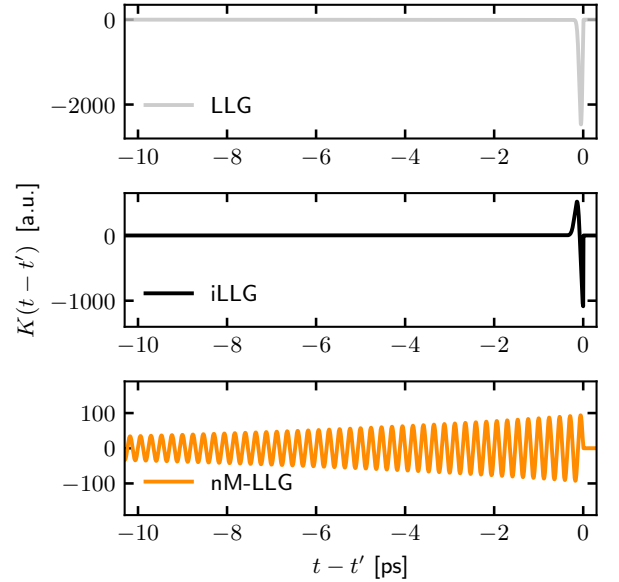


FIG. 12. **Memory kernels in time:** Plot of memory kernels  $K(t - t')$ , which when inserted into Eq.(1), result in the three equations, LLG, iLLG, nM-LLG, respectively. The kernels shown here lead to the Fourier spectra plotted in Fig. 2b. The standard LLG equation is time-local and Markovian. The kernel for the nM-LLG equation has an extended memory time of  $\sim 10$  ps, which leads to non-Markovian dynamics on this timescale.

is given by

$$K(\tau) = \Theta(\tau) \mathcal{A} e^{-\Gamma\tau/2} \frac{\sin(\nu_1\tau)}{\nu_1}, \quad (\text{J1})$$

where  $\tau = t - t'$  and  $\nu_1 = \sqrt{\nu_0^2 - \Gamma^2/4}$ . For the above discussed Lorentzian parameters the kernel is plotted in the bottom panel of Fig. 12.

In Ref. [23] the LLG-limit (time-local, Markovian) of Eq. (1) is discussed. To obtain the desired limit, one chooses a spectral density which is linear in frequency, i.e.  $I(\nu) \propto \alpha\nu$ , where  $\alpha$  is the damping parameter. This leads to the following memory kernel

$$K(\tau) = -\alpha\Theta(\tau)\partial_\tau\delta(\tau - \epsilon_+), \quad (\text{J2})$$

where  $\epsilon_+$  is an infinitesimal positive constant which is set to zero at the calculation's end.

Following a similar logic one can construct a memory kernel which leads to the iLLG equation

$$K(\tau) = \alpha\Theta(\tau) (\partial_\tau\delta(\tau - \epsilon_+) + \tau_{\text{in}}\partial_\tau^2\delta(\tau - \epsilon_+)). \quad (\text{J3})$$

The memory kernel for the LLG and iLLG equation are shown in the top and middle panel of Fig. 12, respectively. For illustrative purposes, the delta functions are approximated by a Gaussian.

## Appendix K: Temperature-dependent simulations

Adding a demagnetization field  $\mathbf{H}_d(t) = -N_{z,0} M_z(t)/M_0 \hat{\mathbf{z}}$  to the bias field  $\mathbf{H}_{\text{bias}} = \hat{\mathbf{x}} \cdot 0.1$  T is a way of introducing the geometry of the film, with  $N_{z,0}$  being the demagnetization field factor at



zero Kelvin. The effect of  $\mathbf{H}_d(t)$  is to counteract any magnetization pointing outside the film, i.e.  $\mathbf{H}_d(t)$  acts whenever there is a non-zero  $M_z$  component. The demagnetization field factor  $N_{z,0}$  is taken for temperature of 0 Kelvin as  $N_{z,0} = 1.37$  T. With increasing temperature, the magnitude of the magnetization,  $\langle M_x \rangle_{\text{eq}}(T)$ , decreases and the counteracting demagnetization field is then proportionally reduced [38], i.e. here  $\mathbf{H}_d(t, T) = -N_T M_z(t)/M_0 \hat{\mathbf{z}}$  with  $N_T = N_{z,0} \frac{\langle M_x \rangle_{\text{eq}}(T)}{\langle M_x \rangle_{\text{eq}}(0)}$ . Here  $\langle M_x \rangle_{\text{eq}}(T)$  is obtained by solving the dynamics to steady state, where  $\langle M_y \rangle_{\text{eq}} = \langle M_z \rangle_{\text{eq}} = 0$ , including the demagnetization field of  $\mathbf{H}_d(t, T = 0K)$ . Second order corrections could be taken into account self-consistently; however, these corrections are negligible here. This yields the following demagnetization field factors for the three simulation temperatures in the main text:  $N_T(\tilde{T} = 20) \approx 0.98 N_{z,0}$ ,  $N_T(\tilde{T} = 220) \approx 0.8 N_{z,0}$ , and

$$N_T(\tilde{T} = 300) \approx 0.73 N_{z,0}.$$

The nM-LLGsimulation is carried out for a single magnetic moment  $M_0$ . This can represent either a single spin or, in the macrospin approximation, an effective moment associated with an ensemble of interacting spins. Due to the mLLG equation only depending on the combined scale  $M_0 T_{\text{sim}}$  [23], the simulation temperature  $T_{\text{sim}}$  corresponding to  $T_{\text{exp}}$  is not specified without knowing the magnetic moment in the macrospin approximation. Knowing this analytically is not feasible – it would require specifying the number of spins, their individual moments and their interactions. Instead of doing so, we set the magnetic moment as  $M_0 = 1\hbar$  and chose the simulation temperature proportionally to the experimental temperature  $T_{\text{sim}} = T_{\text{exp}} c/K$ , with  $c$  a proportionality constant. We choose  $c = 1 \cdot 10^4 \hbar \tilde{\omega}_L / k_B$ . This corresponds to a macrospin length of  $M_{\text{mac}} \approx 1.3 \cdot 10^4 \hbar$ .